JOURNAL OF APPLIED ELECTROCHEMISTRY 25 (1995) 628–641

Real area and electrocatalysis factors in hydrogen evolution kinetics at electrodeposited Ni–Mo and Ni–Mo–Cd composites: effect of Cd content and nature of substrate

R. ŠIMPRAGA, L. BAI,* B. E. CONWAY

Chemistry Department, University of Ottawa, 10 Marie Curie St., Ottawa, K1N 6N5, Canada

Received 25 April 1994; revised 5 December 1994

Electrodeposited Ni–Mo–Cd composites are of considerable practical interest as electrocatalysts for the cathodic production of hydrogen gas in water electrolysers, and as cathode materials for chloralkali and chlorate cells where minimization of electric power consumption is of concern economically. The present work extends the study of the electrocatalytic behaviour of these materials and addresses the influence of cadmium content and the nature of the substrate on which the composites are deposited, particularly with regard to the behaviour and state of **H** species adsorbed during hydrogen evolution. In the case of a carbon-based, gas-diffusion type electrode substrate, the behaviour of the HER on electrodeposited Ni–Mo–Cd is significantly different from that of the same electrodeposit on a nickel substrate.

1. Introduction

The cathodic hydrogen evolution reaction (HER) has been the subject of extensive studies as a prototype of the gas-generation type of electrocatalytic reaction where two ions are discharged and a diatomic gas is produced. Practically, it has become of major commercial importance in relation to the development of advanced fuel-cells, cathodes for the chloralkali process and water electrolysers where polarization performance and power consumption for high current density operation are important economic factors. Additionally, the relation of the HER to **H** sorption into metals has become of substantial interest in metal hydride battery technology [1, 2] and, for D, the process of D sorption into palladium [3].

In general, the electrochemical performance of water electrolysers and chloralkali cells is determined by the polarization of the electrodes and the *IR* drop which originates from the internal resistance of the solution and the electrode configuration. The polarization factor is an intrinsic aspect of the electrode kinetics, determined by the electrocatalytic properties of the electrode, together with the range of operating current densities determined by the real-to-apparent area ratio of its surface [4]; the latter factor is of practical importance in comparative evaluations of apparent electrolytic activities of porous electrode materials.

Previously, we have reported electrocatalytic studies on the HER at Ni [5] and electrodeposited Ni–Mo and Ni–Mo–Cd composites [5–8], glassy-metal Ni–Mo alloys with B, Fe or Cr [9] and bulk Ni–Mo alloys [5, 8, 10] at which hydride phases can arise in the near-surface region of the electrode [7, 9, 14]. Complementary work has been described by Lasia *et al.* [11–13].

In the present paper, we extend the previous examination of electrodeposited Ni–Mo–Cd composites [7, 8] to studies of (a) the role of Cd, codeposited with Ni and Mo, and the influence of its content in the composite on the polarization performance as well as on the **H** adsorption behaviour, and (b) the influence of the substrates for the deposition of the composite on the electrochemical performances of the resulting electrodes for the HER. Three types of measurements, steady state, potential–relaxation and a.c. impedance, were conducted in order to derive information on the electrochemical behaviour of these materials as cathodes for hydrogen production.

2. Experimental details

2.1. *Preparation of the Ni-based composite electrodes*

Ni-based electrodeposited composites with Mo and Cd, used as the working electrodes, are probably microheterogeneous composite structures rather than thermodynamically well-characterized, true alloys. Their preparation was based on a US patent [15], as described in earlier work [5, 7, 8]. Mo is, by itself, not electrodepositable from aqueous solutions. However, in the presence of Ni being electrodeposited, 20–30 at % of Mo (or W or V) can be effectively codeposited, usually with substantial evolution of hydrogen, so that adsorbed and absorbed **H** may play a significant role in this process. Here, for the purpose of improving the apparent current density

* Present address: Motorola, Energy Systems, 4088 Commercial Avenue, Northbrook, IL 60062-1840, USA.

0021-891X

against potential relations for the HER, composites were plated on relatively high-area matrices of carbon ('gas diffusion electrode' material, Alupower Inc., NJ), expanded nickel-mesh ('Exmet' material), spongy nickel ('Cleveite' Ni-battery materials, Cleveland) and fibrous nickel products (Maxwell Laboratories Inc., Auburn, AL) under optimized plating conditions (apparent current density, $j_p = 0.15\,A\,cm^{-2}$, temperature, $T = 325\,K$, and for a duration, $t = 0.5\,h$, with continuous stirring).

2.2. *Morphology and composition determination of the Ni-based composites*

The surface morphology of the Ni–Mo and Ni–Mo–Cd composites was examined by means of an Electro-Scan environmental scanning microscope provided with an energy dispersive X-ray attachment in order to provide near-surface composition analyses of the electrode materials studied.

2.3. *Reference and counter electrodes*

A reversible hydrogen electrode (RHE) in the same solution as that of the working electrode was used as the reference electrode. A platinum gauze, spot-welded onto a platinum wire sealed into a glass tube, was used as the counter electrode.

2.4. *Solution, cell and gases*

The electrolytes employed were aqueous 0.5–4.0 mol dm^{-3} KOH solutions at several temperatures over the range 298 to 348 K. Use of KOH up to 4.0 mol dm^{-3} was required in order to determine (see below) double-layer capacitance values corresponding to a large accessible fraction of the real area of the porous electrode matrices using principles based on the model experiments described in [4].

A conventional three-compartment all-glass cell, provided with glass sleeved stopcocks, so that it could be immersed in a thermostat without contamination of the solution, was used to conduct all measurements.

Purified hydrogen gas was bubbled continuously, at 1 bar pressure, through the working and reference electrode compartments.

2.5. *Methods*

To study the kinetics of hydrogen evolution and sorption behaviour of the kinetically involved species in the process, three types of measurements were carried out: steady-state, potential–relaxation and a.c. impedance, as follows.

2.5.1. Potentiostatic, steady-state cathodic polarization. Tafel relations were recorded by means of a PAR 173 potentiostat controlled by a Hewlett–Packard 87 microcomputer with a Kepco SN 488 122 programmer and a Keithley model 195 A/D convertor. First, to reduce any oxide film initially present at the electrode surface, and obtain a well-defined initial potential, electrodes were cathodically prepolarized at −0.3 V for an hour prior to commencement of the steady-state measurements over the temperature range 298 to 348 K. Such measurements were carried out in both ascending and descending directions of change of the potential, using a staircase waveform software, with increments of 5 mV and a polarization duration of 60 s at each overpotential. This procedure resulted in very good reproducibility of recorded Tafel relations and other derived data, and precise control of the polarization conditions.

2.5.2. Potential-relaxation transients. Potential–relaxation transients were recorded from various corresponding cathodic overpotentials following interruption of respective prior steady-state polarizing currents by means of a mercury contact relay switch [6]. Potential against time transients over 5 to 6 decades of time (cf. [6]) were recorded digitally by means of a Nicolet digital oscilloscope and stored on a floppy disk for further analysis. The polarizing potentials of the working electrode were kept at desired values until the currents attained the same respective values as those corresponding to previously determined Tafel relations recorded prior to the transient experiments. The potential–decay transients were then initiated and recorded. Several transients were recorded for each electrode studied, within the potential range −0.25 to −0.05 V at 298 K. The potential relaxation and complementary polarization data were processed, as described in earlier papers [4, 5–8, 16, 17], using a Hewlett–Packard 9000 computer and software developed in this laboratory.

2.5.3. Real surface area determination. The real electrode surface area was evaluated from *in situ* measurements of double-layer capacitance, determined from initial potential–decay slopes, $(d\eta/dt)_{t=0}$ following interruption of significant, overpotential (η)-dependent, faradaic currents:

$$j(\eta) = j_0 \exp\left(\frac{\alpha\eta F}{RT}\right) \tag{1}$$

passing across the electrode/electrolyte interface. The method employed (see below) was developed in our laboratory recently and quantitatively validated [4], and is based on the recording and analysis of the initial region of the potential-relaxation transient, i.e. over a short time range, where the interfacial capacitance corresponds [17] to the double-layer self-discharge process. As explained earlier, above, KOH electrolyte concentrations up to 4.0 mol dm^{-3} are required (cf. [4]) to minimize the effect of distributed resistance in the porous electrode structure on the derived double-layer capacitance values.

The potential–relaxation behaviour, recorded immediately after interruption of the polarization current, $j(t = 0)$, is determined [18] by the potential–decay relation:

$$-C\frac{d\eta}{dt} = j(\eta) = j_0 \exp\left(\frac{\alpha\eta F}{RT}\right) \tag{2}$$

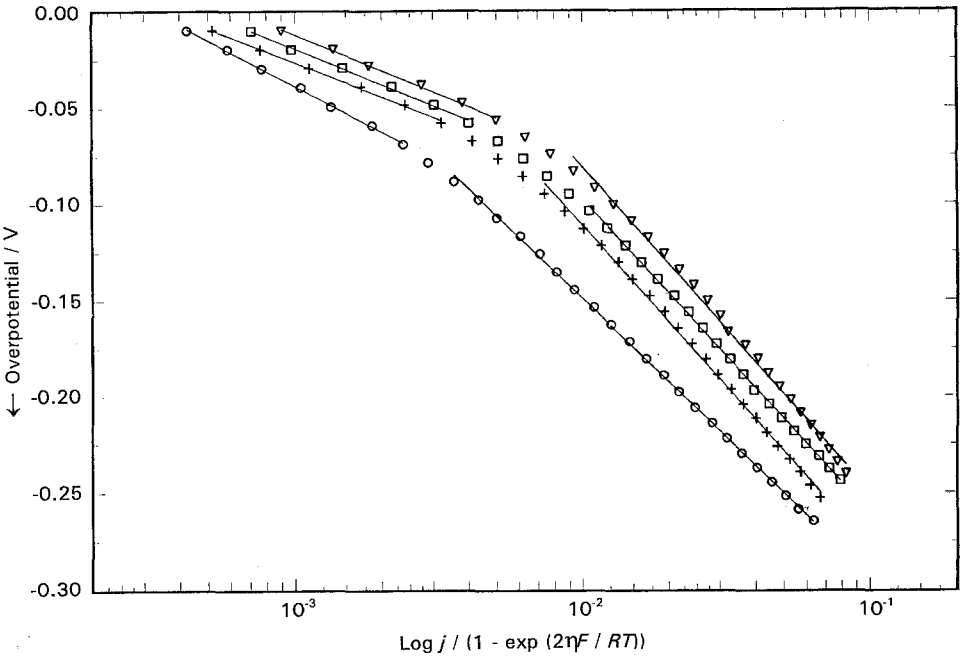

Fig. 1. Tafel plots for the HER at Ni–Mo and Ni–Mo–Cd coated electrodes, with different $[Cd^{2+}]$, at 298 K and 1 h polarization at −0.3 V. $[Cd^{2+}]$: (○) 0.0, (+) 1.5×10^{-4}, (□) 7.5×10^{-4} and (▽) 1.5×10^{-3} mol dm^{-3}.

where j_0 represents the exchange current density, α the transfer coefficient and C is the interfacial capacitance. Integration of Equation 2, for the case where C is constant, gives

$$\eta(t) = a - b\log(t + \tau) \tag{3}$$

where $a = -b\log(2.3j_0/bC)$, $b = 2.3RT/\beta F$ and τ (an integration constant [6, 7]) $= bC/2.3j(t = 0)$. Therefore $\eta(t)$ for $t \gg \tau$ should be a linear function of $\log t$ and from Equation 2,

$$C = \frac{j(t = 0)}{(-\mathrm{d}\eta/\mathrm{d}t)_{t=0}} \tag{4}$$

where $j(t = 0)$ is recorded experimentally at each potential for which current interruption is made. C, corresponding to the interfacial capacitance at the overpotential, $\eta(t = 0)$, at which the initial steady-state current is passing, can be calculated from Equation 4 if the initial potential–decay slope $(-\mathrm{d}\eta/\mathrm{d}t)_{t=0}$ could be reliably determined. As it is not easy to determine this accurately by simply drawing a tangent to the η against t curve at $t = 0$, the following procedure was proposed and validated [4]; differentiating Equation 3 with respect to t, gives

$$\left(\frac{\mathrm{d}\eta}{\mathrm{d}t}\right)_{t=0} = -\frac{b}{2.3\tau} \tag{5}$$

The method [4] involves the following steps: (i) the η as a function of t data are digitally recorded after interruption of the polarization current; (ii) the η against t data are fitted to Equation 3 by means of a nonlinear least-squares fitting procedure (using EXCEL software) which gives the best values for the constants a, b and τ for each recorded $\eta(t)$ transient; (iii) from these constants, $(-\mathrm{d}\eta/\mathrm{d}t)_{t=0}$ can be calculated from Equation 5 giving C from Equation 4. Comparing the values for C thus calculated with a recently determined [4] value of the double-layer capacitance of a smooth bright platinum electrode ($C_{dl} = 25\,\mu\mathrm{F\,cm^{-2}}$) of true area known from UPD **H** accommodation determined by cyclic voltammetry [4], it was possible to evaluate the real surface areas of the electrodes studied, or the real to apparent surface area ratio, $\mathscr{R}$.

2.5.4. A.c. impedance spectroscopy. The a.c. impedance measurements were conducted by means of a Solartron 1255 HF frequency response analyser in conjunction with a computer-controlled PAR 273 potentiostat, using the commercially available electrochemical software, ZPLOT. A sinusoidal signal, 10 mV r.m.s. in amplitude, was applied in the measurements conducted at several d.c. potentials over a potential range −0.2 to −0.01 V at 298 K. A PC and the LEVM software, based on the 'complex nonlinear least squares immittance' fitting procedure developed by Ross Macdonald [19], were used for the data analyses.

2.5.5. IR drop corrections. To correct the Tafel polarization data for *IR* drop effects, the uncompensated solution resistance values were calculated from data acquired from the a.c. impedance and potential–decay measurements. Values of 0.1 to 0.5 Ω, obtained by both methods, over the temperature range 298 to 348 K, were used for these *IR* corrections.

3. Results and discussion

3.1. *Introduction*

From earlier work [7, 8] on electrodeposited Ni–Mo–Cd electrodes, it was concluded that: (a) they exhibit good polarization performance which arises, in part, from a low Tafel slope region which persists increasingly to higher current densities as the

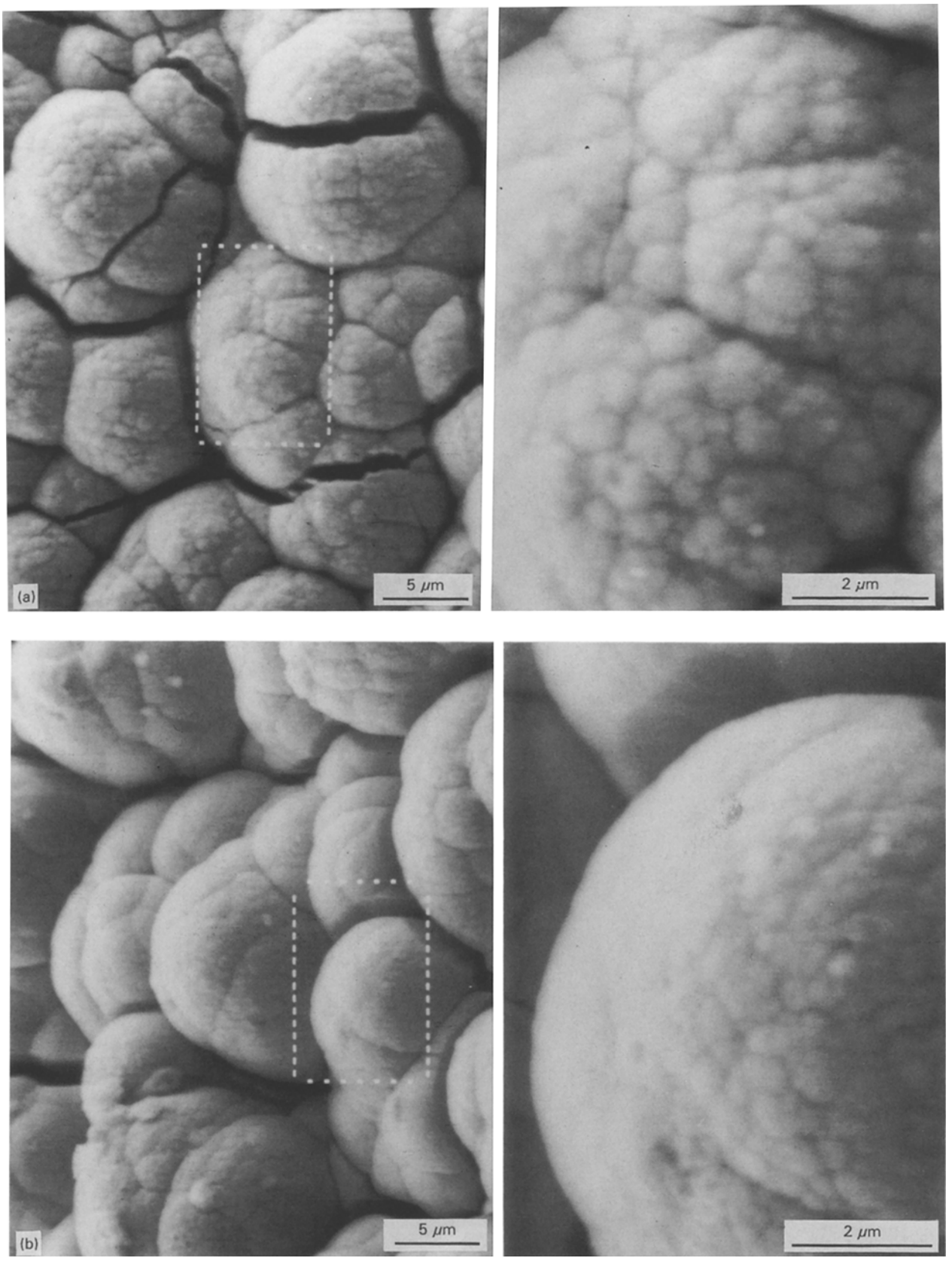

temperature is raised, and is associated with a region of appreciable **H**-sorption pseudocapacitance, i.e. the coverage is potential dependent; and (b) the behaviour of these electrode materials differs in some fundamental ways from that of metallic Ni and bulk, single-phase Ni–Mo alloys, so the favourable polarization performance is not due simply to the large ratio of real-to-apparent areas that are normally the result of the Ni–Mo codeposition procedure [7, 8], although this is a substantial factor in the favourable polarization performance achieved with these materials.

The first question that arises is the extent to which an amount of ~1% Cd in the composite has influence

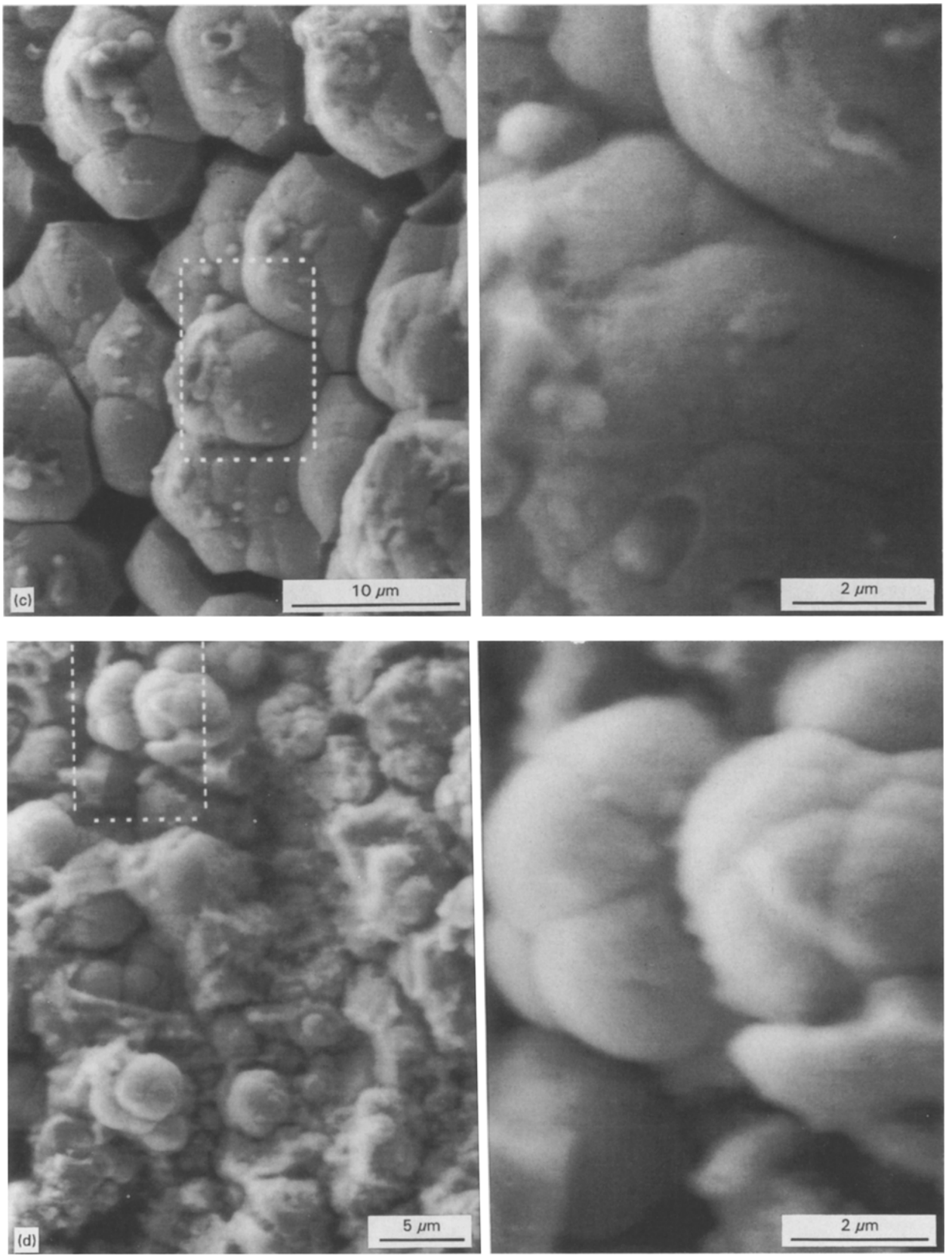

Fig. 2. ESEM micrographs of the electrode materials used for the HER in Fig. 1: (a) Ni–Mo and Ni–Mo–Cd with different $[Cd^{2+}]$; (b) 1.5×10^{-4} mol dm^{-3}, (c) 7.5×10^{-4} mol dm^{-3} and (d) 1.5×10^{-3} mol dm^{-3}.

on the electrochemical behaviour of the composites and what is its role. A further question is how to improve the polarization performance of the electrode materials for practical use. Therefore, two approaches were chosen in the present work: (i) an examination, quantitatively, of the influence of Cd and (ii) the influence of the substrate employed for the deposition of the composites on the electrochemical behaviour of the resulting electrode materials in terms of HER polarization characteristics.

3.2. *Role of Cd in the electrodeposited Ni–Mo–Cd composites*

To examine the role of Cd in the Ni–Mo–Cd composite on the polarization behaviour of the HER, experiments were conducted at ten electrodes, having five different compositions, that had been prepared under the same plating conditions, but with variation of the concentration of Cd^{2+} in the plating solution between 0 and 10^{-2} mol dm^{-3}.

The hydrogen evolution reaction is assumed to take place through the usual well-known steps in the reaction mechanism for alkaline solutions where H_2O is the proton source.

3.2.1. Steady-state behaviour. The steady-state overpotential (η) against log(current density, j) plots for the HER at 298 K, corrected for *IR* drop as well as for the back-reaction current component at low η values, at Ni–Mo and three Ni–Mo–Cd electrodeposits formed on a nickel-rod substrate, are shown in Fig. 1. Two regions of Tafel slope are observed in all cases. In the high current-density region, the observed slopes of -120 ± 2 mV dec^{-1} for Ni–Mo and -135 ± 3 mV dec^{-1} for Ni–Mo–Cd are associated with a charge transfer process as the rate-controlling step in distinction from the chemical recombination step. However, the low current-density region slope of -73 ± 2 mV dec^{-1} for Ni–Mo and about -48 ± 2 mV dec^{-1} for Ni–Mo–Cd, which would arise due to significant (potential-dependent) **H** adsorption at the materials studied, suggests that a rate-controlling step other than the initial discharge step itself [7, 8], i.e. one following it, determines the kinetics.

Figure 1 also shows that increase of the Cd^{2+} concentration in the plating solution yields a more active electrode for the HER, although for Cd^{2+} concentrations $>10^{-3}$ mol dm^{-3}, no further change in polarization behaviour arose, which may correspond to a limiting cadmium content that can be co-deposited with nickel and molybdenum, or change of the Ni/Mo ratio in the resulting materials.

Adding 1.5×10^{-4} mol dm^{-3} of Cd^{2+} to the plating solution gave rise to an increase of about 2× in current at $\eta = -0.150$ V. A further increase in Cd^{2+} concentration up to 1.5×10^{-3} mol dm^{-3} increased this current only by an additional ~40% (in 2 × 20% increments), as shown in Fig. 1. The initial increase in current density due to the presence of cadmium could arise either from an increase in the real surface area and/or from changes in intrinsic electrocatalytic activity for the HER.

3.2.2. Environmental scanning electron microscopy (ESEM) and energy dispersive X-ray spectroscopy (EDX) results. Figure 2 shows ESEM micrographs of (a) the Ni–Mo and (b), (c) and (d) of the Ni–Mo–Cd composites used as cathodes for the present HER studies, at two comparative magnifications of 2000× and 8000×, respectively.

Table 1. Results of EDX analyses of electrodeposited Ni–Mo–Cd composites

$[Cd^{2+}]$/mol dm^{-3}	0.0	1.5×10^{-4}	7.5×10^{-4}	1.5×10^{-3}
Ni	70	79.6	86.5	91.7
Mo	30	20.4	13.3	6.1
Cd	0.0	>0.1	<1	1.6

The ESEM micrographs (Fig. 2(a) and (b)) show that the overall deposit morphology is not significantly changed by the presence of 1.5×10^{-4} mol dm^{-3} Cd^{2+} in the plating solution and appears, in both cases, to consist of nodular 'cauliflower-like' structures with about 10 μm diameter 'heads'. If anything, the 'cauliflowers' that arise in the presence of Cd^{2+} appear somewhat smoother with small nuclei of further 'cauliflower' features visible. This suggests that the increase in current may not be due simply to increased surface area alone, and is consistent with values of the double-layer capacitance, 0.020 to 0.028 F cm^{-2}, found for both these types of electrodes from impedance and potential relaxation measurements (see below).

The ESEM micrographs of the deposits obtained from the 7.5×10^{-4} and 1.5×10^{-3} mol dm^{-3} Cd^{2+} solutions are shown in Fig. 2(c) and (d) which indicates that the further increase of Cd^{2+} in the plating solution strongly influences the surface morphology of the resulting electrode materials. Note that increase of Cd^{2+} concentration beyond the 1.5×10^{-3} mol dm^{-3} does not result in greater activity of the electrode materials for the HER, as noted in 3.2.1.

EDX analyses of the first micrometre or so of the surface of the electrode materials are given in Table 1. The average cadmium content in the composites was generally <1 at%, except for the electrode plated from the solution most concentrated in Cd^{2+} (1.5×10^{-3} mol dm^{-3}), where the average cadmium level was determined to be 1.6 at%. Despite this small extent of incorporation of cadmium into the deposits, the Ni/Mo ratio was found to be very sensitive to the presence or effect of small concentrations of Cd^{2+} in the plating solution and thus of the amount of cadmium coplated. In the absence of a large difference in real surface area between the two types of electrodes, as determined by means of the impedance spectroscopy and potential relaxation measurements, the appreciable improvements in the polarization behaviour (Fig. 1) appear to be related significantly to the Ni/Mo content in the deposit, which is found to be substantially influenced by the Cd^{2+} present in the plating solution (see Table 1). This effect may arise from a change of current efficiency for Ni + Mo deposition due to an effect of deposited Cd on the kinetics of coevolution of hydrogen gas, i.e. partial current density for the latter process or its current efficiency.

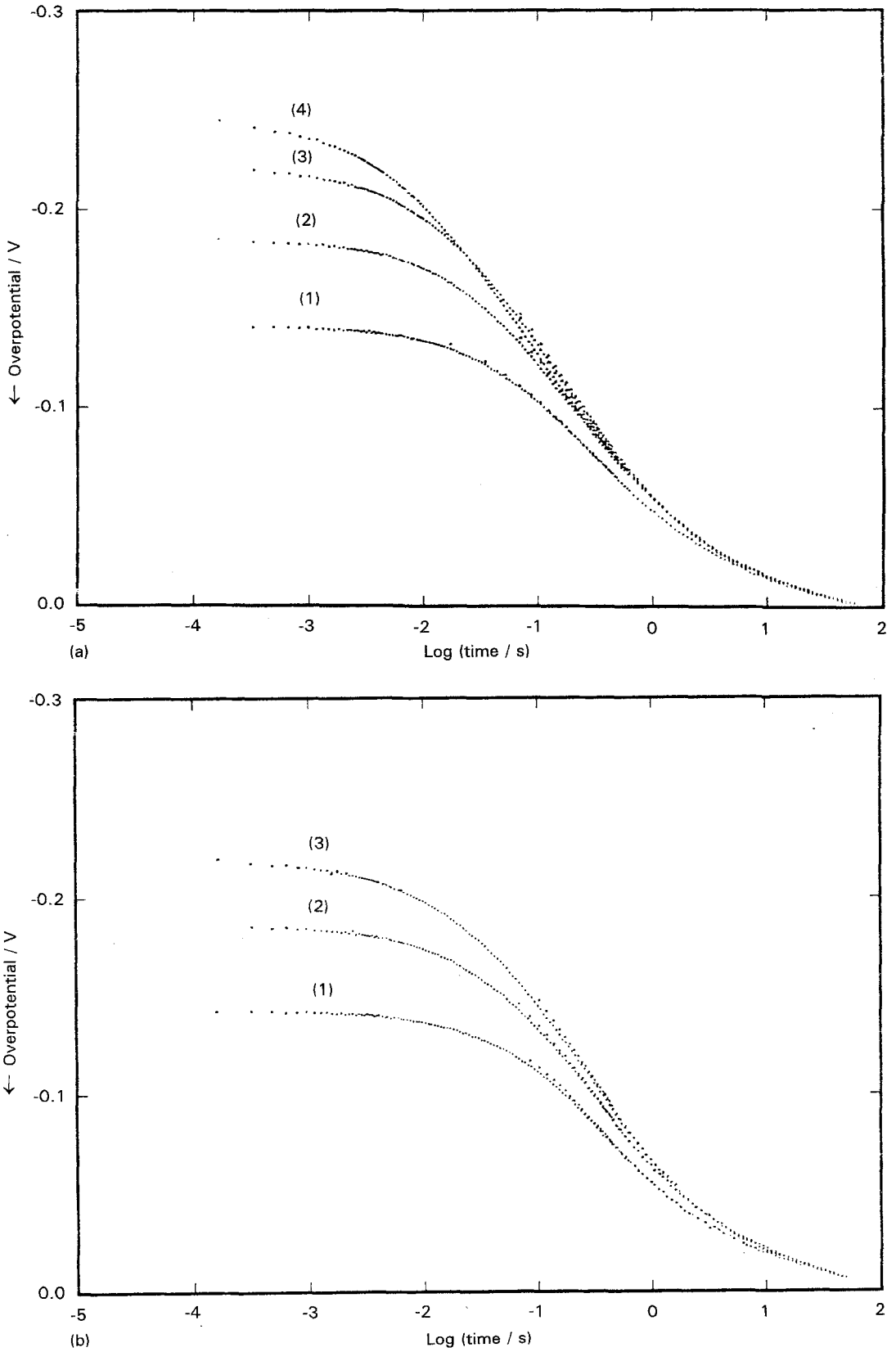

Fig. 3. Overpotential, η, against log time, t plots for the HER at (a) Ni–Mo and (b) Ni–Mo–Cd coated electrodes recorded after interruption of polarization at four over-potentials: (1) −0.15, (2) −0.20, (3) −0.25 and (4) −0.30 V at 298 K. Note that the curve for Ni–Mo–Cd from $\eta = -0.3$ V was not recorded due to hydrogen bubbles remaining on the electrode surface.

3.2.3. Potential-relaxation behaviour. Potential relaxation, as well as a.c. impedance measurements, were recorded consecutively for each electrode that was examined potentiostatically. The transients were taken from various overpotentials along the corresponding Tafel line upon interruption of successively established steady cathodic currents, as explained earlier. The potential decay data were processed directly in terms of $d\eta/dt$, giving information on the η-dependent interfacial capacitance [6,

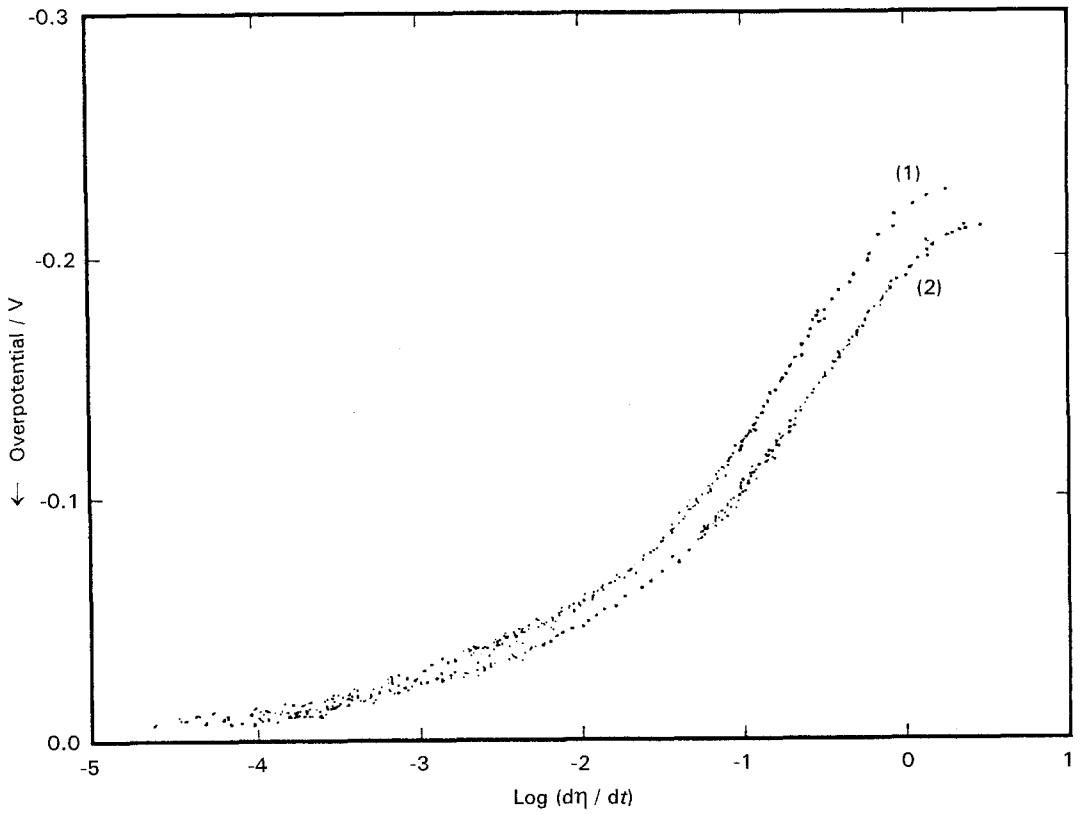

Fig. 4. Comparison of the η against $\log(-d\eta/dt)$ plots for the HER at Ni–Mo (1) and Ni–Mo–Cd (2) coated electrodes at 298 K.

17, 18, 20, 21], expressed formally by Equation 6:

$$j(t) = j_0 \exp\left(\frac{\alpha\eta F}{RT}\right) = -C\left(\frac{d\eta}{dt}\right)$$

$$= -(C_{dl} + C_\phi)\frac{d\eta}{dt} \qquad (6)$$

where C_{dl} is the double-layer capacitance and C_ϕ the apparent pseudocapacitance associated with η-dependent coverage of sorbed H species, and possible hydride oxidation (cf. [5]).

In the present work, directed to practical examination of the performance of various Ni–Mo and Ni–Mo–Cd electrode structures, Equation 6 was employed for the purpose of comparative evaluation of these materials through determination of apparent $C_{dl} + C_\phi$ values and their potential dependence, as well as the $\eta(t)$ against $\log(-d\eta/dt)$ behaviour as treated in [6] and [7]. The fuller kinetic treatment of such potential–relaxation transients that can be made on the basis of [17] or [22] was not considered necessary for the purposes of the present paper.

In Fig. 3(a) and (b) we first show the potential relaxation curves, plotted logarithmically in time (cf. [6]), for Ni–Mo and Ni–Mo–Cd, respectively, taken

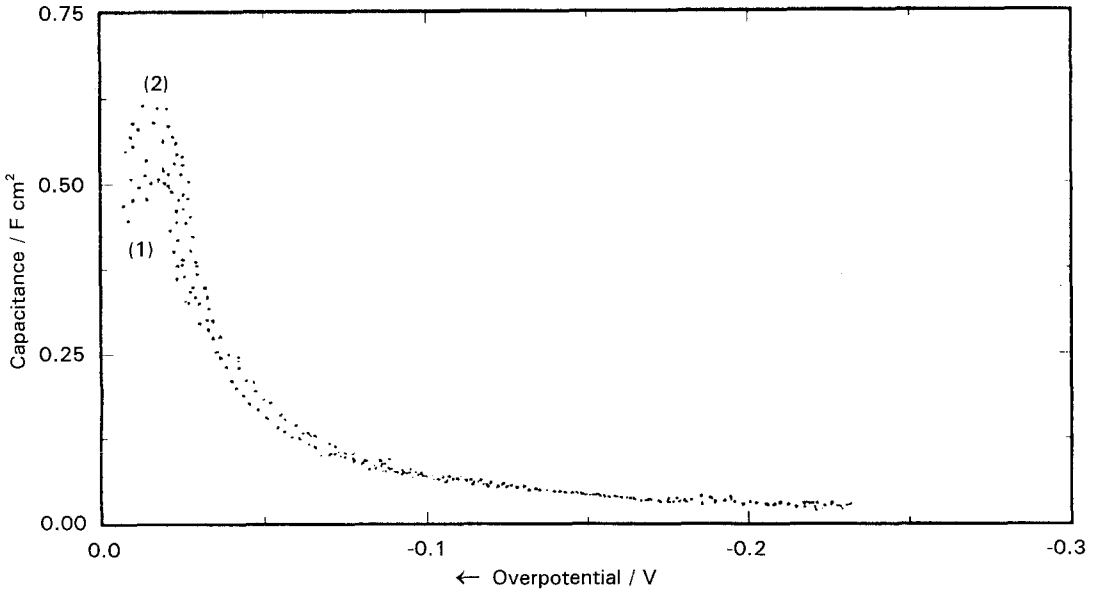

Fig. 5. Comparison of the capacitance against overpotential plots for Ni–Mo (1) and Ni–Mo–Cd (2) coated electrodes at 298 K.

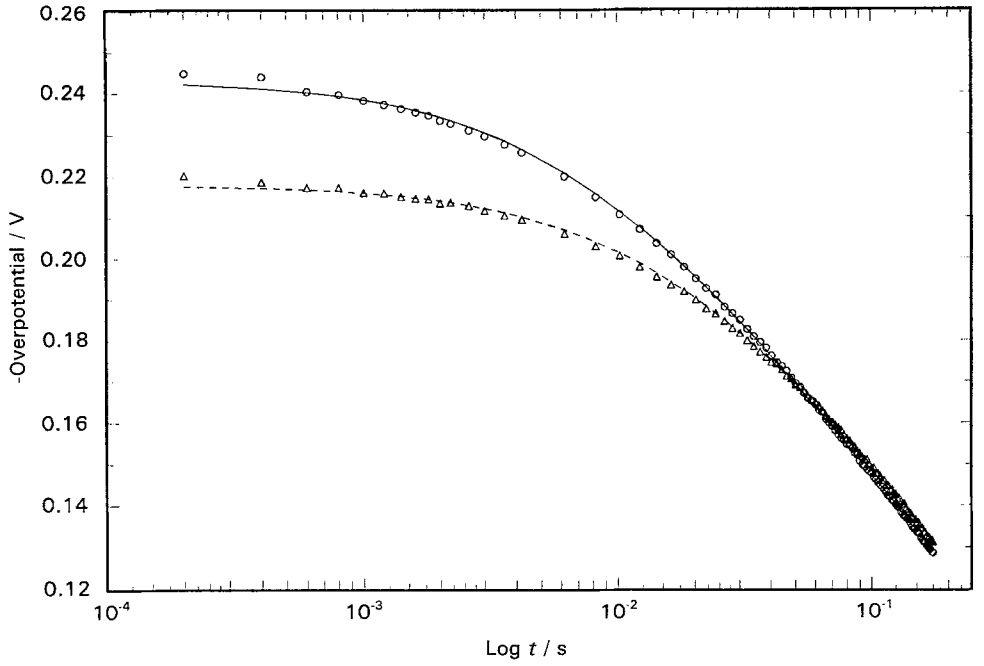

Fig. 6. Experimental (symbols) and fitted (lines) potential decay curves in the initial, short-time range for the HER at Ni–Mo–Cd at 298 K. Key: (○) −0.300 V; (——) −0.300 V fit; (△) −0.250 V; (– – – –) −0.250 V fit.

Table 2. Evaluated real/apparent surface area, $\mathscr{R}$, from C_{dl} values for Ni–Mo and Ni–Mo–Cd composite materials derived from the initial potential–decay rate method

Electrode	η/V	j/A cm^{-2}	$-(d\eta/dt)_{t=0}$	C_{dl}/mF ± 1	$\mathscr{R}$ ± 5%
Ni–Mo	0.30	5.40×10^{-2}	2.51	21.5	858
	0.25	3.57×10^{-2}	1.61	22.3	893
Ni–Mo–Cd	0.30	1.04×10^{-1}	5.01	20.9	836
	0.25	5.44×10^{-2}	2.39	22.9	912

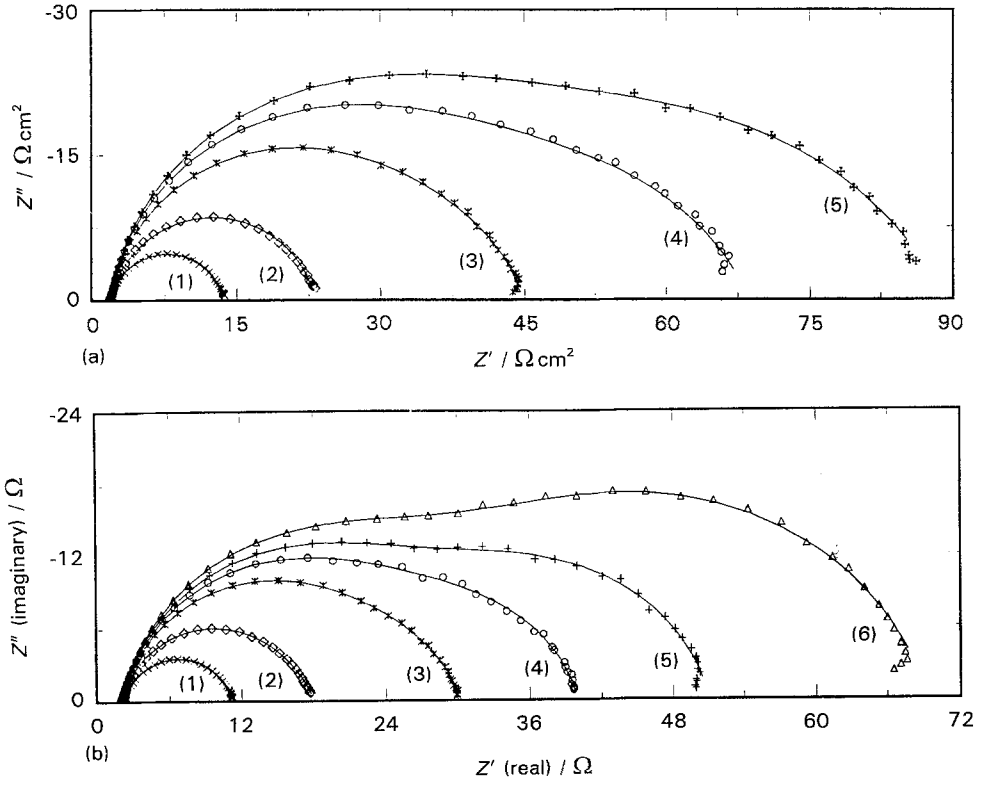

Fig. 7. Experimental (symbols) and fitted (solid lines) complex-plane plots of impedance for the HER at Ni–Mo (a) and Ni–Mo–Cd (b) coated electrodes at 298 K, recorded at several d.c. potentials: (1) −0.15, (2) −0.1, (3) −0.05, (4) −0.03, (5) −0.02 and (6) −0.01 V. Ranges of ω as on Fig. 8(a) and (b).

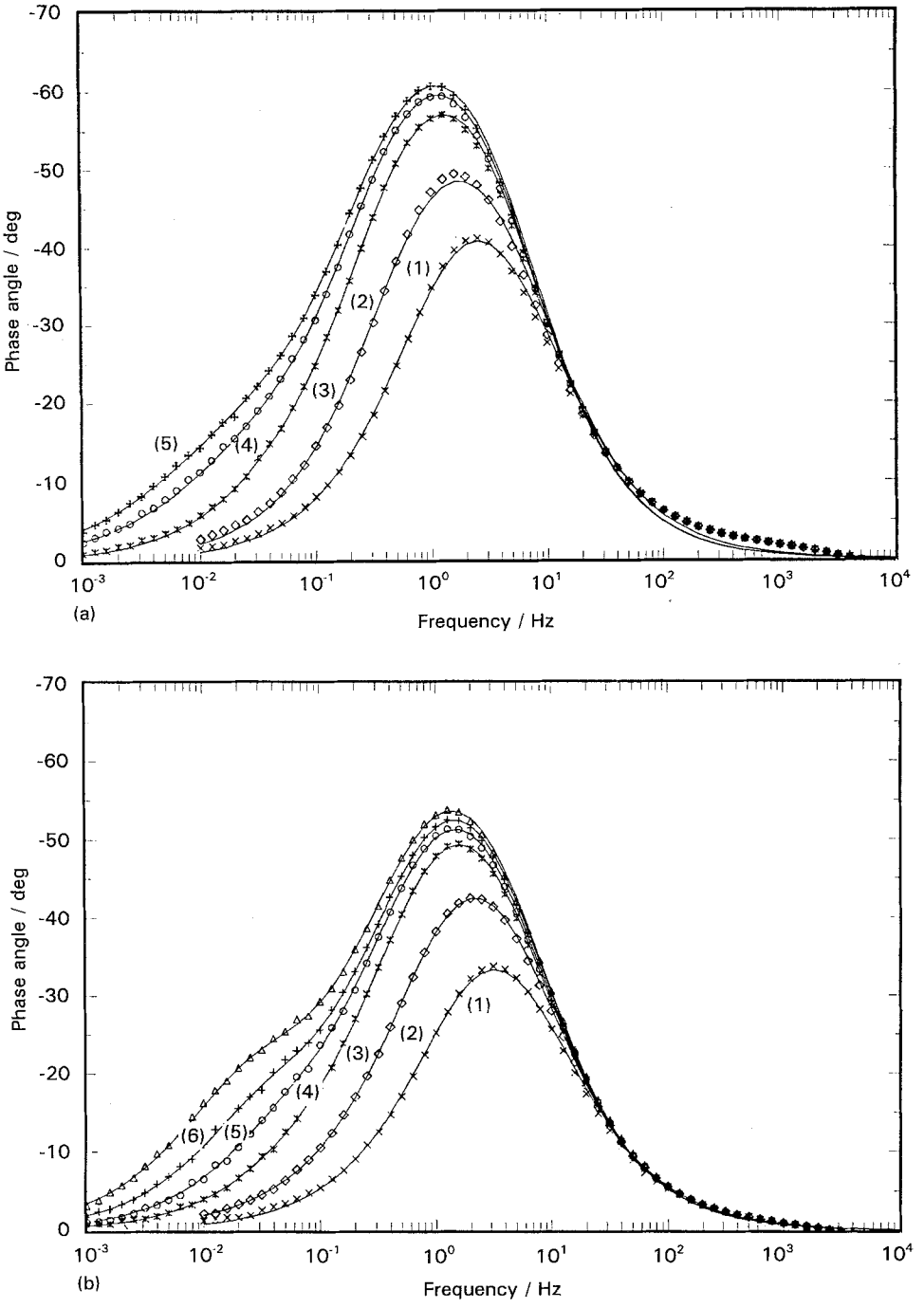

Fig. 8. Experimental (symbols) and fitted Bode phase-angle plots for the HER at Ni–Mo (a) and Ni–Mo–Cd (b) coated electrodes at 298 K, recorded at several d.c. potentials: (1) −0.15, (2) −0.1, (3) −0.05, (4) −0.03, (5) −0.02 and (6) −0.01 V.

from several overpotentials at 298 K. It is seen that there are two slope regions in the η against $\log t$ relations for both cases.

As discussed elsewhere [6, 7], it is also informative to plot $\eta(t)$ against $\log(-\mathrm{d}\eta/\mathrm{d}t)$ values derived from the $\eta(t)$ transients, as shown in Fig. 4. As in the above Tafel and η against $\log t$ relations, two distinguishable slopes are exhibited, one at small t's and high η ($-100\,\mathrm{mV\,dec^{-1}}$) and the other over longer t's and small η's ($20 \sim 40\,\mathrm{mV\,dec^{-1}}$).

The overall interfacial capacitance against η relations for the HER at Ni–Mo and Ni–Mo–Cd are shown in Fig. 5. For short times, the relaxation transient $\eta(t)$ is determined principally by $C \equiv C_{\mathrm{dl}}$, the interfacial double-layer capacitance [17].

When the coverage, θ, of adsorbed intermediate is η-dependent, C involves the adsorption pseudo-capacitance, as defined by $C_\phi = q_1(\mathrm{d}\theta/\mathrm{d}\eta)$ for the steady-state coverage, where q_1 is charge for the adsorption/desorption of an hypothetical monolayer of an intermediate, here **H**. C_ϕ dominates the potential–decay behaviour at lower overpotentials (-10 to $-80\,\mathrm{mV}$) and sufficiently long times when $C_\phi \gg C_{\mathrm{dl}}$, as discussed in [7] and [17]. Note that Fig. 5 shows that there is no significant difference in the *form* of the C against η relations for the Ni–Mo and Ni–Mo–Cd electrocatalysts.

3.2.4. Analysis of initial slopes of η against log t curves. The procedure for fitting of experimental initial

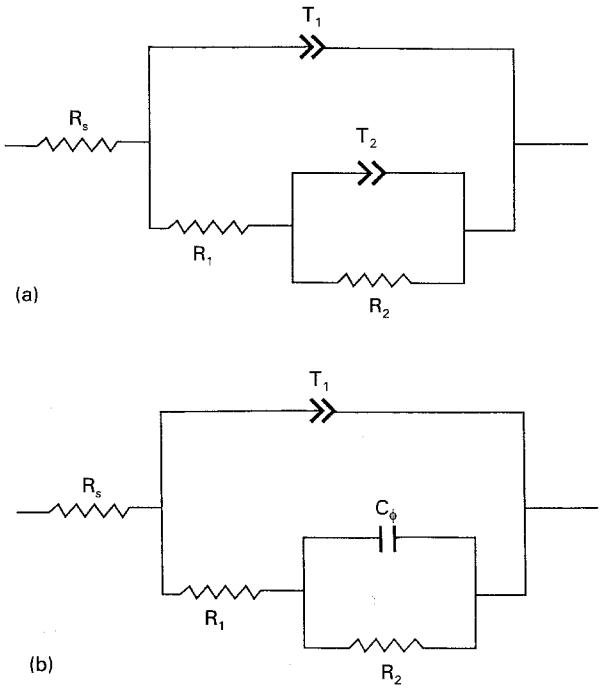

Fig. 9. Equivalent circuits used for simulation the experimental a.c. impedance behaviour in 0.5 mol dm^{-3} KOH (a) and in 4.0 mol dm^{-3} KOH (b).

potential–decay data was described in Section 2.5.3. Figure 6 shows experimental (symbols) and fitted (lines) open-circuit potential–relaxation curves over an initial time range, for the HER at the electrodeposited Ni–Mo–Cd composite in 0.5 mol dm^{-3} KOH, at 298 K, taken for two initial potentials. What is to be considered as the 'initial' part (cf. [4]) of the potential relaxation curve is determined by the τ value (Equation 3). For the present high-area electrodes τ is much larger than for corresponding smooth electrodes. The results derived from Fig. 3(a) and (b) are listed in Table 2, together with the real/apparent surface area ratios, R, derived from the C_{dl} values.

3.2.5. A.c. impedance behaviour. Important complementary information is provided by means of a.c. impedance spectroscopy [17, 22, 23] conducted not only as a function of frequency but also of applied 'd.c.' overpotential (cf. [24]). The results are conveniently represented in terms of complex-plane plots (Fig. 7(a) and (b)) and Bode-type plots of phase-angle against $\log\omega$ (Fig. 8(a) and (b)) recorded at several overpotentials in the range covered in Fig. 1.

For both the Ni–Mo and Ni–Mo–Cd materials, only one semicircle in the complex-plane and one peak in the phase-angle against $\log\omega$ plots is exhibited between $\eta = -0.1$ and -0.3 V. However, at lower η (-0.01 to -0.1 V) a second semicircle as well as a second peak in the phase-angle plot develops, which are better separated (Fig. 7(a) and (b)) for the Ni–Mo–Cd than for Ni–Mo electrode; also, the faradaic resistance is smaller than for the Ni–Mo composite (cf. the Tafel and $\eta(t)$ behaviour). All the semicircles in Fig. 7(a) and (b) are 'depressed' below the $Z'' = 0$ axis, a characteristic of porous electrodes [25], the impedance of which is commonly represented by a 'constant phase element' (CPE) in the equivalent circuit [25].

3.2.6. Simulation of frequency-response behaviour. The frequency response of an electrochemical reaction can

Table 3. The best-fit values of the equivalent circuit elements of Fig. 9 for the data shown in Fig. 7(a) and (b)

Electrode σ/% →	*Curve*	$-E$/V	R_1/Ω *<1*	T_1/F^{φ} *1*	φ_1 *1*	R_2/Ω *2*	T_2/F^{φ} *1–4*	φ_2 *1*
Ni–Mo	(1)	0.15	12	0.020	0.85	–	–	–
(Fig. 7)	(2)	0.10	38	0.020	0.88	1.3	0.095	0.81
	(3)	0.05	35	0.020	0.89	7.4	0.33	0.72
	(4)	0.03	43	0.019	0.90	24	0.17	0.79
	(5)	0.02	4	0.018	0.90	40	0.13	0.80
Ni–Mo–Cd	(1)	0.15	9	0.021	0.84	–	–	–
(Fig. 8)	(2)	0.10	15	0.021	0.86	1.05	0.068	0.80
	(3)	0.05	24	0.021	0.86	3.9	0.523	0.82
	(4)	0.03	28	0.020	0.87	1	0.29	0.83
	(5)	0.02	30	0.022	0.87	19	0.229	0.82
	(6)	0.01	33	0.019	0.87	34	0.163	0.79

Table 4. Evaluated kinetic parameters for the HER from Tafel plots for Ni–Mo–Cd composites on various substrates

Substrate	*Tafel slope, b* / mV dec^{-1} *low j*		*high j*		*Current density, j* / mA cm^{-1} $\eta = -100$ mV		$\eta = -200$ mV	
	298 *K* ±2	348 *K* ±1	298 *K* ±2	298 *K* ±2	298 K ±1	348 K ±1	298 K ±1	348 K ±1
Ni-rod	37	31	118	120	1.1	38.5	8.2	123
Fibrous nickel	47	42	115	120	3.6	49.5	12.3	190
Gas-diffusion electrode	35	28	125	120	33.1	178	105	393

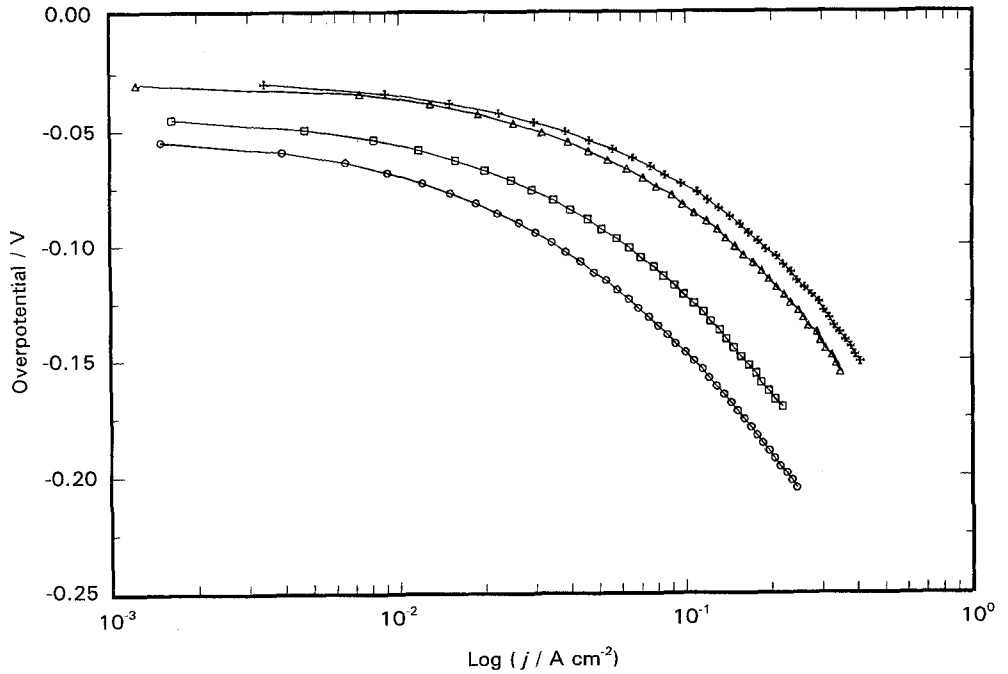

Fig. 10. Tafel plots for the HER at Ni–Mo–Cd electrodeposited on the 'gas diffusion electrode' substrate recorded at four temperatures: (○) 298, (□) 313, (△) 333 and (+) 348 K.

be simulated either by a rationally chosen equivalent circuit [25] as in Fig. 9(a) and (b), or by fitting the observed frequency-response behaviour in terms of the reaction steps of the mechanism and their respective rate constants [11, 13, 17, 22, 23, 26 and 27].

For the fitting of the experimental behaviour by the first procedure, the circuit in Fig. 9(a) was employed. A CPE (represented empirically by $Z_{CPE} = 1/T(j\omega)^{\varphi}$; for $\varphi = 1$, $T \equiv C_{dl}$), was used to effect the fitting of the complex-plane plots at various η values. Based on this approach, the frequency-response behaviour of the HER, shown in Fig. 7(a) and (b) and in Fig. 8(a) and (b), could be well represented as shown by the solid lines in relation to the experimental data (indicated by symbols) for various η and over a wide (10^{-3} to 10^{4} Hz) ω range. The values of 'best fit' to the equivalent circuit elements of Fig. 9(a), for the data shown in Fig. 7(a) and (b), are listed in Table 3, wherein are also recorded overall standard deviations (%) for the data in columns 4–9.

The experimental and fitted impedance results (Table 3) indicate that for $\eta < -0.1$ V, where the adsorption of the H intermediate is appreciable and η-dependent, $C_{\phi(H)} \gg C_{dl}$. However, for $\eta > |0.1|$ V, less or no response from $C_{\phi(H)}$ arises, corresponding to little or no $d\theta_H/d\eta$ at the higher η's.

To optimize the Ni–Mo–Cd electrode performance and improve the current densities per apparent cm^2 of projected area of the electrodes, electrode performance evaluations were extended to an examination of these materials deposited on several *different* substrates, in more concentrated alkaline electrolytes, in the temperature range 298 to 348 K.

3.3. *Influence of the substrate for the composite deposition on the electrochemical behaviour of resulting cathode materials*

Since the Ni–Mo–Cd coatings are more active for the HER than is Ni–Mo alone, behaviour of the

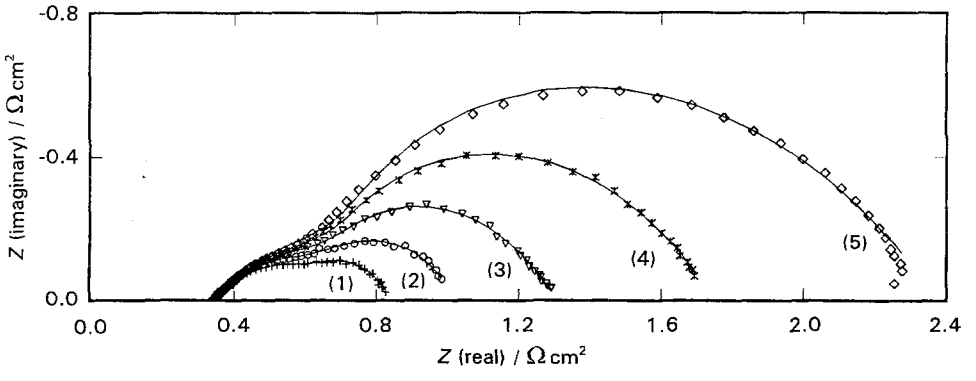

Fig. 11. Experimental (symbols) and fitted (solid lines) complex-plane plots of impedance for the HER at Ni–Mo–Cd electrodeposited on the 'gas diffusion electrode' substrate, recorded at five overpotentials: (1) −0.2, (2) −0.17, (3) −0.14, (4) −0.11 and (5) −0.08 V.

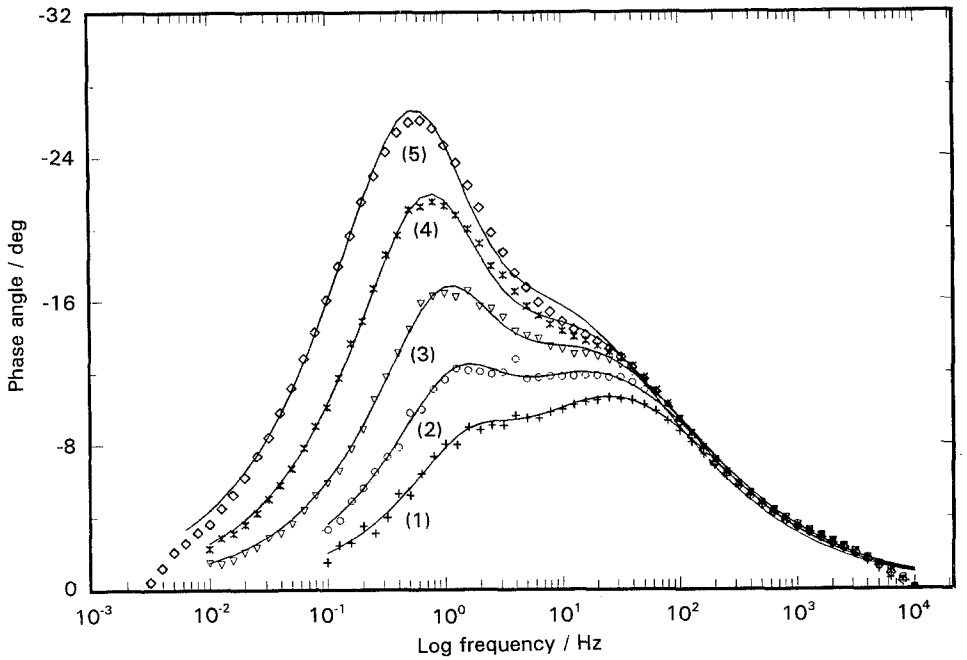

Fig. 12. Experimental (symbols) and fitted Bode phase-angle plots for the HER at Ni–Mo–Cd electrodeposited on the 'gas diffusion electrode' substrate, recorded at five overpotentials: (1) −0.2, (2) −0.17, (3) −0.14, (4) −0.11 and (5) −0.08 V.

former materials deposited on the following, commercially available, high area, substrates was examined: (a) a spongy Ni, (b) a fibrous Ni, (c) a Ni 'Exmet' grid and (d) a 'gas-diffusion electrode', that is, a carbon-based, fuel-cell type of high-area material (Alupower, NJ). Steady-state and a.c. impedance measurements were conducted at the resulting coated substrate materials.

3.3.1. Steady-state behaviour. As above, the electrocatalytic performance for hydrogen evolution was evaluated on the basis of Tafel polarization plots over the range of $j = 10^{-4}$ to 5×10^{-1} A per apparent cm^2 in 4.0 mol dm^{-3} KOH at several temperatures between 298 and 348 K. Table 4 records comparative data at 298 and 348 K for substrates (b) and (d) above in comparison with a Ni-rod. At the higher temperatures, very favourable performance is achieved for the 'gas diffusion electrode' as substrate, as shown in Fig. 10. At 348 K, apparent current densities of about 0.2–0.3 A cm^{-2} can be realized at a nominal practical operating overvoltage of only −100 mV. Even at 298 K, 60 mA cm^{-2} can be realized at $\eta = -100$ mV (Fig. 10).

3.3.2. A.c. impedance behaviour. Complex-plane and phase-angle plots were recorded at several overpotentials over the range covered in the Tafel plots of Fig. 10 at 298 K and are shown in Figs 11 and 12, respectively. The solid lines represent the fittings (based on the equivalent circuit of Fig. 9(b)) of the behaviour and the experimental data are represented by the symbols, as indicated in Figs 11 and 12.

It is interesting that the impedance behaviour of the electrocatalyst deposited on the 'gas-diffusion' electrode is quite different from that for the *same* catalyst deposited on the nickel-based substrates. Two distinct semicircles in the complex-plane plots and two well separated peaks in the phase-angle against $\log \omega$ relations are exhibited over the whole η range corresponding to the Tafel relations in Fig. 10.

For fitting of the frequency response data in Figs 11 and 12, the procedure already described above was employed and the best-fit values for the equivalent circuit (Fig. 9(b)) elements are recorded in Table 5, with standard deviations, as in Table 3. These results show that C_ϕ dominates the a.c. behaviour, although it varies with η. The high values of the C components arise, presumably, on account of the high real-to-

Table 5. The best-fit values of the circuit elements of Fig. 9(a) for the data shown in Figs 11 and 12

Curve σ/% →	$-\eta$/V	R_1/Ω *1*	T_1/F^{φ} *1*	φ *1*	R_2/Ω *2*	C_ϕ/F *1–8*
(1)	0.20	0.37	0.17	0.61	0.11	0.27
(2)	0.17	0.46	0.19	0.58	0.21	0.30
(3)	0.14	0.54	0.20	0.58	0.42	0.38
(4)	0.11	0.62	0.22	0.58	0.78	0.56
(5)	0.08	0.61	0.21	0.57	1.37	1.11

apparent surface area ratios that can be achieved by electrodeposition on to the gas diffusion electrode as substrate.

4. Conclusions

(i) The Ni–Mo–Cd composites are more active for the HER than the Ni–Mo material.
(ii) Increase of the Cd^{2+} concentration from 0.0 to $1.5\,mol\,dm^{-3}$ in the plating solution yields electrode materials that are more active for the HER, although for concentrations $>10^{-3}\,mol\,dm^{-3}$ little further increase in activity arises.
(iii) The ESEM micrographs and EDX analyses show that the cadmium content in the electrodeposits does not increase proportionally with increasing Cd^{2+} concentration in the plating solution, but the Ni/Mo content ratio is substantially influenced by $[Cd^{2+}]$ change.
(iv) The latter behaviour is likely to be due to an effect of cadmium on current efficiency *vis-à-vis* hydrogen production.
(v) Deposition of Ni–Mo–Cd on the high surface area, 'gas-diffusion electrode' results in the greatest activity for the HER and a unique a.c. impedance behaviour.

Acknowledgements

Grateful acknowledgements are made to the Natural Sciences and Engineering Research Council of Canada and to Alcan International Ltd for support of this work through the NSERC/Alcan Industrial Chair at University of Ottawa held by B. E. Conway. Thanks are also due to S. Y. Qian and L. Gao of this laboratory for help with the computer simulations, to D. Tessier of Alcan International for his interest in this project and to Donald H. Klosterman of Motorola, Corporate Manufacturing Research Center, for performing the ESEM and EDX analyses.

References

[1] M. A. Fetschenko, S. Venkatasan, S. R. Ovshinsky and M. Hirota, Proceedings of the International Battery Association Conference, Seattle, WA (1990), Int. Battery Association, Washington, DC (1991).
[2] B. E. Conway and G. Jerkiewicz, *J. Electroanal. Chem.* **357** (1993) 47.
[3] F. G. Will, K. Cedzynska and D. C. Linton, *ibid.* **360** (1993) 161.
[4] L. Bai, L. Gao and B. E. Conway, *J. Chem. Soc., Faraday Trans.* **89**(2) (1993) 235.
[5] B. E. Conway, H. Angerstein-Kozlowska, M. A. Sattar and B. V. Tilak, *J. Electrochem. Soc.* **130** (1983) 1825.
[6] B. E. Conway, L. Bai and D. F. Tessier, *J. Electroanal. Chem.* **161** (1984) 39.
[7] B. E. Conway and L. Bai, *J. Chem. Soc., Faraday Trans.* **81** (1985) 1841.
[8] *Idem, Int. J. Hydrogen Energy* **11** (1986) 533.
[9] Lj. Vračar and B. E. Conway, *J. Electroanal. Chem.* **277** (1990) 253.
[10] R. Brousseau, PhD. thesis, University of Ottawa, Ottawa, Canada (1989).
[11] A. Lasia and A. Rami, *J. Electroanal. Chem.* **294** (1990) 123.
[12] P. Los, A. Lasia and H. Menard, *ibid.* **360** (1993) 101.
[13] P. Los and A. Lasia, *J. Appl. Electrochem.* **23** (1993) 135.
[14] B. E. Conway and L. Bai, *J. Electroanal. Chem.* **198** (1986) 149.
[15] N. Stachurski, D. Pouli, G. Pokrzyk and J. Rinas, *US Patent 4354915*, to Occidental Petroleum, Research Center, Grand Island, New York (1982).
[16] B. E. Conway and L. Bai, *Electrochimica Acta* **31** (1986) 1013.
[17] D. A. Harrington and B. E. Conway, *J. Electroanal. Chem.* **221** (1987) 1.
[18] J. A. Butler and J. F. Armstrong, *Trans. Faraday Soc.* **29** (1933) 1261.
[19] J. R. Macdonald, private communication.
[20] H. H. Ewe, *Electrochim. Acta* **17** (1972) 2267.
[21] A. G. C. Kobussen, H. Willems and G. H. Broers, *J. Electroanal. Chem.* **142** (1982) 67.
[22] R. D. Armstrong and M. Henderson, *ibid.* **39** (1982) 81.
[23] L. Bai, D. A. Harrington and B. E. Conway, *Electrochim. Acta* **32** (1987) 1713.
[24] L. Bai and B. E. Conway, *J. Electrochem Soc.* **137** (1990) 3737.
[25] J. R. Macdonald, *in* 'Impedance spectroscopy', (edited by J. R. Macdonald), Wiley, New York (1987) pp. 47–59.
[26] J. E. B. Randles, *Disc. Faraday Soc.* **1** (1947) 11.
[27] M. Sluyters-Rehbach and J. H. Sluyters, 'Electroanalytical chemistry', vol. 4 (edited by A. J. Bard), Marcel Dekker, New York (1970), chapter 1.